CIRP Annals - Manufacturing Technology 72 (2023) 301–304

Contents lists available at ScienceDirect

CIRP Annals - Manufacturing Technology

journal homepage: https://www.editorialmanager.com/CIRP/default.aspx

Vision-based thermal drift monitoring method for machine tools

Gregory W. Vogl[a,*], Ainsley Rexford[b], Zongze Li[c], Robert G. Landers[c], Edward C. Kinzel[c], M. Alkan Donmez (1)[a], Joe Chalfoun[d]

[a] Engineering Laboratory, National Institute of Standards and Technology (NIST), 100 Bureau Drive, Gaithersburg, Maryland 20899-8220, USA
[b] School of Engineering and Applied Sciences, University of Pennsylvania, Philadelphia, Pennsylvania 19104, USA
[c] Department of Aerospace and Mechanical Engineering, University of Notre Dame, Notre Dame, Indiana 46556, USA
[d] Information Technology Laboratory, National Institute of Standards and Technology (NIST), 100 Bureau Drive, Gaithersburg, Maryland 20899-8220, USA

A R T I C L E I N F O

Article history:
Available online 15 April 2023

Keywords:
Thermal error
Machine tool
Monitoring

A B S T R A C T

A method is presented to measure machine tool thermal drift for error compensation. A wireless microscope within a tool holder in the spindle is used to capture videos of image targets attached to the worktable. For each target, one video is captured during spindle rotation orthogonal to the worktable and another video is captured during axis translation orthogonal to the worktable. Data are collected periodically so that the three-dimensional thermal error at each target location is determined via image analysis. Experiments verify that the method measures micrometer-level tool-to-workpiece thermal drift for error model development and thermal drift compensation.

Published by Elsevier Ltd on behalf of CIRP.

1. Introduction

Temperature variations within a machine tool due to internal heat generation and heat transfer with the environment cause thermal deformations that may lead to dimensional errors of a machined workpiece [1]. In fact, dimensional deviations of machined parts can be mainly attributed to thermally-induced displacements [2], especially for large-volume components [3]. Because thermal errors may account for up to 75 percent of the total geometrical errors of a machined part [1], advances in machining performance require the reduction of thermal errors.

The reduction of thermal errors is usually achieved through (1) machine design for thermal management, (2) an integrated model for prediction and correction, or (3) real-time measurement and compensation of thermal errors. However, few approaches are efficiently implemented on both existing and new machine tools. First, machine design for thermal management, e.g., with a cooling system [4] or non-metallic spindle materials [5], is generally expensive. Second, an integrated model to predict and correct thermal errors, e.g., with machine parameters and sensed temperatures inputted into a model [6], is inherently difficult to develop because of the metrological effort and complexity [7,8]. Third, a thermal compensation process [9,10] is typically difficult to achieve with quick, accurate, and inexpensive intermittent measurements [1]. Other approaches include machining process optimization [3], camera measurements and work volume-sized grids of crossed lines [11], and a thermal displacement estimation method using temperature sensor data with deep learning [12].

Thus, a new method is needed for thermal drift monitoring and compensation of machine tools that is fast, accurate, inexpensive, non-invasive, and practical for industrial adoption. This paper introduces such a method for monitoring of tool-to-workpiece thermal variations and demonstrates its experimental validation.

2. Method

Fig. 1 shows a high-level overview of the proposed method for real-time monitoring of tool-to-workpiece thermal drift. A wireless microscope within the spindle captures videos to determine local three-dimensional thermal drifts of the spindle with respect to multiple high-contrast image targets located on the worktable. These local drifts are then used in a model to estimate the thermal drift within the work volume.

The microscope transmits videos of multiple targets to a smartphone for data capture. The targets have markings with relatively high contrast for image analysis purposes. For any thermal state, one rotation video and one vertical translation video are captured at each target in less than half a minute. Each rotation video yields the change in local planar (X-axis and Y-axis) displacements when its

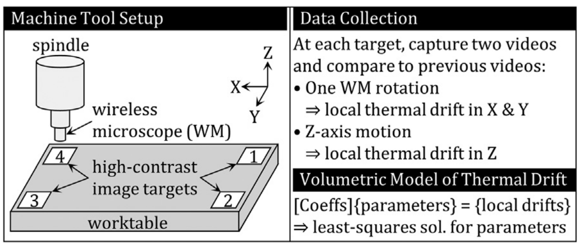

Fig. 1. Overview of tool-to-workpiece thermal drift monitoring method.

* Corresponding author.
E-mail address:

https://doi.org/10.1016/j.cirp.2023.04.053
0007-8506/Published by Elsevier Ltd on behalf of CIRP.

analysis results are compared to those of the target's previous thermal state, while each translation video yields the change in local out-of-plane (Z-axis) displacement when its analysis results are compared to those of the target's previous thermal state. The following subsections explain these processes.

2.1. Spindle rotation to determine in-plane displacements

At each target, a rotation video is captured with the spindle rotating at a sufficiently slow speed, such that each video frame avoids motion blur to maintain sufficient contrast. The video for the i^{th} thermal state is then analyzed to yield the spindle rotation center, C_i, in the machine coordinate frame, as explained next.

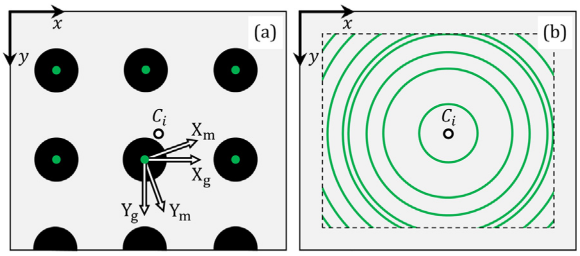

Fig. 2. Schematic of (a) image of calibration dot grid and (b) tracks of all calibration dot centers in a rotation video.

One useful high-contrast image target is a grid of black dots with a known grid spacing, as seen in Fig. 2a. The grid of dots has its own local coordinate frame, (X_g, Y_g), and the machine tool has its own local coordinate frame, (X_m, Y_m), both of which rotate about C_i in the image pixel frame, (x, y), as the microscope rotates. C_i was positioned to be close to a chosen dot center, so that even with thermal drift, C_i remains closest to that same dot center (the chosen origin of the local frames). As shown in Fig. 2b, the dot centers for all images in the rotation video can be plotted together, revealing nominally circular tracks with center C_i. A custom segmentation-and-tracking routine [13] is utilized to locate and track each dot center from image to image. Note that each rotation video should capture at least one full rotation of the microscope, so that the arcs are as circular as possible for fitting purposes. While one arc may establish C_i, multiple arcs aid the fitting process (see below) and a dot grid establishes X_g and Y_g in each image. Also, only the centers of full dots were utilized; partial dots with centers outside the dashed box in Fig. 2b were ignored.

The rotation center, C_i, is then determined by fitting circular arcs of various radii and one common center to the arcs of Fig. 2b. Every point (x, y) of the q^{th} arc should satisfy the equation for a circle, $(x - x_C)^2 + (y - y_C)^2 = {R_q}^2$, where (x_C, y_C) is the location of C_i in the image pixel frame and R_q is the pixel radius of the q^{th} arc. Rearrangement into matrix form yields

$$[-2x \quad -2y \quad 1]\left[x_C \quad y_C \quad {x_C}^2 + {y_C}^2 - {R_q}^2\right]^T = -(x^2 + y^2) \tag{1}$$

By utilizing every point for all arcs, a linear system of equations is formed from Eq. (1) to solve for x_C, y_C, and the radii via the least-squares method. Hence, the rotation center, C_i, is known in the image pixel frame. One significant advantage of a rotating microscope is that C_i is independent of misalignment and drift of the camera optical axis relative to the spindle rotation axis.

Next, transformation of C_i from pixel coordinates to local machine coordinates uses the known grid spacing, the average grid spacing in pixels, and the relationship between the local machine frame and the local grid frame measured *a priori* via the same routine [13] used on videos of X-axis or Y-axis translation at each target. Finally, the change of C_i in machine coordinates from one thermal state to another yields the local in-plane thermal drift.

2.2. Translation to determine out-of-plane displacement

At each target, one translation video is captured with the spindle moving at a constant velocity along the Z-axis with the motion of length L centered around the nominal Z-axis position. The out-of-plane displacement is determined via an analysis that involves computing the contrast of each image, calculated using a Gaussian derivative method [14]. A Gaussian convolution kernel, $\Gamma(\hat{x}, \hat{y})$, for a pixel $(\hat{x}, \hat{y})$ within a square pixel window with an edge length of $2N_w$ is defined as

$$\Gamma(\hat{x}, \hat{y}) = \frac{1}{2\pi\sigma} \exp\left(-\frac{\hat{x}^2 + \hat{y}^2}{2\sigma^2}\right), \quad \begin{cases} -N_w \le \hat{x} \le N_w \\ -N_w \le \hat{y} \le N_w \end{cases} \tag{2}$$

where $\sigma = N_w/2.5$ and $N_w = 7$, which were chosen to yield a $\Gamma(\hat{x}, \hat{y})$ that has decayed much near the window edges. For the i^{th} thermal state, the pixel contrast value φ_{ik} at any pixel $(x,\ y)$ of the k^{th} image is calculated by convolution with the kernel as

$$\begin{aligned} \varphi_{ik}(x,\ y) = &\left[\sum_{\hat{x}=-N_w}^{N_w} \sum_{\hat{y}=-N_w}^{N_w} \Gamma_x(\hat{x}, \hat{y}) g_{ik}(x - \hat{x}, y - \hat{y})\right]^2 \\ &+ \left[\sum_{\hat{x}=-N_w}^{N_w} \sum_{\hat{y}=-N_w}^{N_w} \Gamma_y(\hat{x}, \hat{y}) g_{ik}(x - \hat{x}, y - \hat{y})\right]^2 \end{aligned} \tag{3}$$

where Γ_x and Γ_y are the partial derivatives of $\Gamma(x, y)$ with respect to x and y, respectively, and $g_{ik}(x, y)$ is the grayscale intensity value (an integer from 0 to 255) at pixel location (x, y). The magnitude of the grayscale value $g_{ik}(x, y)$ is strongly affected by a microscope-mounted light emitting diode (LED) ring.

The contrast metric ϕ_{ik} is the mean of all φ_{ik} over the k^{th} image with pixel lengths of N_x and N_y in the respective directions; that is,

$$\phi_{ik} = \frac{1}{N_x N_y} \sum_{x=1}^{N_x} \sum_{y=1}^{N_y} \varphi_{ik}(x,\ y) \tag{4}$$

Hence, for a video consisting of K images, the vector ϕ_i of contrast metric values is $\phi_i = [\phi_{i1}, \phi_{i2}, \cdots, \phi_{iK}]$. Fig. 3a shows a schematic of the contrast metric versus image number. The image numbers k_S and k_E denote the start and end of motion, respectively. The relative Z-axis position, Z_k, as a function of image number is then defined as

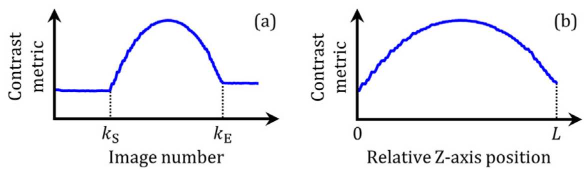

Fig. 3. Contrast metric versus (a) video image number or (b) relative Z-axis position during motion.

$$Z_k = L\frac{k - k_S}{k_E - k_S}, \quad k_S \le k \le k_E \tag{5}$$

so that the contrast is a function of Z, as seen in Fig. 3b.

The local out-of-plane thermal drift from the first thermal state to another thermal state is determined by comparing the two contrast metric curves, ϕ_1 and ϕ_i. Due to deviations in lighting conditions during the measurement process, the contrast metric curves are scaled relative to each other. Thus, for a fair comparison, ϕ_i is scaled relative to ϕ_1 as

$$\hat{\phi}_i = \frac{\max(\phi_1)}{\max(\phi_i)} \phi_i \tag{6}$$

The two curves, ϕ_1 and $\hat{\phi}_i$, as functions of Z should come from the same microscope imaging process, which means ϕ_1 and $\hat{\phi}_i$ should be extremely similar except for a shift in Z due to thermal changes. This deviation, ΔZ_i, is the displacement shift of $\hat{\phi}_i$ that best aligns it to ϕ_1, as shown in Fig. 4.

To determine ΔZ_i, the root mean square (RMS) of the differences between ϕ_1 and $\hat{\phi}_i$ for a variable shift, ΔZ, is first calculated within an overlap range. This range is the intersection of the middle 80 percent of the Z-axis motion ranges for ϕ_1 and $\hat{\phi}_i$ for ΔZ, to eliminate potential transient data at the start and end of each motion. Therefore, the local

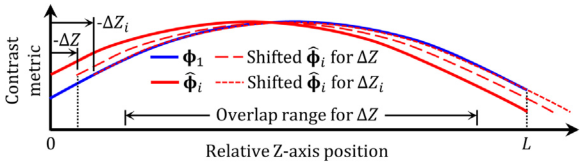

Fig. 4. Original and shifted contrast metric curves.

out-of-plane thermal drift, ΔZ_i, for the i^{th} thermal state is

$$\Delta Z_i = \underset{\Delta Z}{\text{argmin}}\,[\mathbf{RMS}_i(\Delta Z)] \tag{7}$$

where $\mathbf{RMS}_i(\Delta Z)$ is the vector of RMSs for the tested ΔZ values. The negative sign ("-") in Fig. 4 yields the correct sign for ΔZ_i.

3. Thermal drift model

For three-axis machine tools, the proposed linear error model is

$$\mathbf{e} = \mathbf{S}\,\mathbf{E} \tag{8}$$

where $\mathbf{e} = [\Delta x, \Delta y, \Delta z]$ is the volumetric errors, and $\mathbf{E}$ and $\mathbf{S}$ are, respectively, the error parameters and sensitivities defined as

$$\mathbf{E} = [\Delta E_X, \Delta E_Y, \Delta E_Z, \Delta E_A, \Delta E_B, \Delta E_C, \Delta E_{X0Y}, \Delta\alpha_X, \Delta\alpha_Y] \tag{9a}$$

$$\mathbf{S} = \begin{bmatrix} 1 & 0 & 0 & 0 & 0 & -Y_T & -Y_T & X_T & 0 \\ 0 & 1 & 0 & 0 & 0 & X_T & 0 & 0 & Y_T \\ 0 & 0 & 1 & Y_T & -X_T & 0 & 0 & 0 & 0 \end{bmatrix} \tag{9b}$$

where ΔE_X, ΔE_Y, and ΔE_Z are the positional error changes, ΔE_A, ΔE_B, and ΔE_C are the angular error changes, ΔE_{X0Y} is the squareness error change between the X- and Y-axes, $\Delta\alpha_X$ and $\Delta\alpha_Y$ are the linear thermal expansion changes of the X- and Y-axes, respectively, and (X_T, Y_T) are the machine coordinates of the target used during data collection.

According to Eqs. (8)-(9b), three linear equations are obtained from a target. Data are acquired from four targets denoted T1 to T4, and the error parameters $\mathbf{E}$ are computed via least-squares for

$$[\mathbf{e}_{T1}, \mathbf{e}_{T2}, \mathbf{e}_{T3}, \mathbf{e}_{T4}] = [\mathbf{S}_{T1}, \mathbf{S}_{T2}, \mathbf{S}_{T3}, \mathbf{S}_{T4}]\,\mathbf{E} \tag{10}$$

Note that at least three targets are required for a unique solution, while four or more targets give redundancy or the ability to use a different linear or nonlinear model with more error parameters.

4. Experimental setup

Fig. 5 shows the experimental setup used to test the thermal drift tracking method. Four targets (T1 to T4) are attached near the worktable corners (see Fig. 5a). Each target is an ivory-colored calibration artifact composed of a 25 mm × 25 mm grid of black dots with a nominal diameter of 250 µm and a grid spacing of 500 µm. Epoxy with a relatively low coefficient of thermal expansion (54×10^{-6} K^{-1}) is used to attach each artifact into an aluminum alloy part fixtured to the worktable. For the capture of videos of the targets, an inexpensive (< 50 USD) wireless microscope is fixed inside a stainless-steel adapter (see Fig. 5b). The microscope outputs videos to a smartphone with images of 1920 pixels × 1080 pixels at a frame rate of about 13 Hz. The magnification was fixed at about 2.6, yielding pixels that represent a field of view of the target area of about 1.07 µm × 1.07 µm.

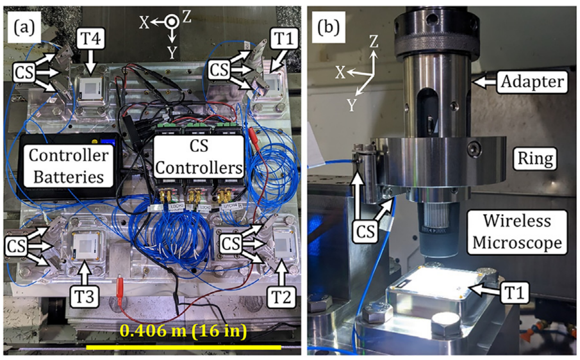

Fig. 5. (a) Experimental setup with four targets (T1 to T4) and twelve capacitive sensors (CSs) and (b) wireless microscope in custom adapter.

Capacitive sensors (CSs) were also set up for verification and validation (V&V) of the new method. As seen in Fig. 5a, three CSs were configured orthogonally within a sensor nest at each of the four targets to measure the local three-dimensional drift. Each CS measured its displacement from a stainless-steel ring (see Fig. 5b) attached to the adapter with the spindle oriented at an angle to eliminate various influences, including the total indicated runout (about 12 µm) measured off the curved ring surface.

At each target, (1) CS data were collected at 25 Hz for 10 s, (2) the rotation video was captured with the spindle rotating at 10 rpm for slightly more than one full rotation, and (3) the translation video was captured with the non-rotating spindle moving in the positive Z-axis direction over 508 µm ($L = 0.02$ in) for 12 s. All data analysis was then performed on a computer.

5. Results

Various experiments were conducted for V&V of the thermal drift tracking method. In each of the following tests, the displacements determined by the CS data are compared against the displacements calculated from the new method, and the errors are the method values minus the CS values.

5.1. Simulated thermal drift

The machine tool and the experimental setup remained near a thermal equilibrium during three different cases of simulated thermal drift: (Case 1) X-axis displacements, (Case 2) simul-taneous X-axis and Y-axis displacements, or (Case 3) simultaneous X-axis, Y-axis, and Z-axis displacements, with data collected at axis displacements from 0 µm to 50.8 µm (0.002 in) with an increment of 10.16 µm (0.0004 in).

Fig. 6 shows histograms (60 occurrences each) of all the combined errors from all three cases. Most error magnitudes for the X- and Y-axis directions are within 1 µm. A separate study for this work revealed that the radial errors of the circular fits (see Section 2.1) are typically within 1 µm with a standard deviation of about 0.27 µm, even with an induced microscope-to-target tilt of more than 500 µrad. Thus, no significant distortion of the dot paths was observed during motion. Also, the effect of the rotation on the sub-pixel radial errors was investigated for various spindle speeds, revealing that the rotation rate of 10 rpm does not significantly affect the measurement uncertainty via the microscope properties (pixel resolution, exposure time, and frame rate). Finally, Fig. 6 shows that most error magnitudes for the Z-axis direction are within 5 µm.

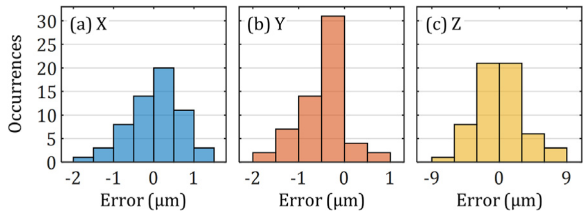

Fig. 6. Histograms of errors of the new method in the (a) X-, (b) Y-, and (c) Z-axis directions for all three simulated thermal drift tests.

5.2. Real thermal drift

The spindle was warmed up at 10k rpm for 30 min without the microscope assembly in it. After the spindle was stopped, the

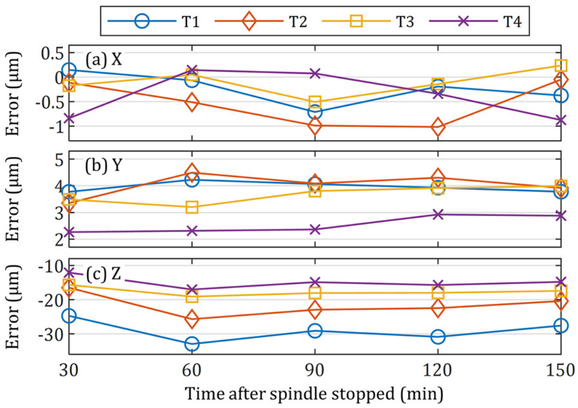

Fig. 7. Errors of the new method in the (a) X-, (b) Y-, and (c) Z-axis directions during spindle cooldown at each of the four targets (T1 to T4).

microscope assembly was placed back into the machine tool and data was collected every 30 min. Fig. 7 shows the errors of the new method for displacements at each thermal state (at 30 min, 60 min, etc.) compared to the initial state (at 0 min). While the X- and Y-axes error magnitudes are within 5 μm, there are significant Z-axis error magnitudes between 10 μm and 35 μm at all targets. The CS data confirmed that the displacements (not shown) in the X-, Y-, and Z-axis direction grew to be only about 7 μm, 10 μm, and 9 μm, respectively, so the Z-axis errors are relatively large. Thermal changes of the microscope affected the errors in the Z-axis direction because the spindle warmed up the microscope after reinsertion.

The machine tool was then in a cooled state before the X-axis was warmed via rapid motion of the axis back and forth over its entire travel range for 30 min. Fig. 8 shows the reference displacements, measured from the cooled state to the warmed state, and the errors of the new method. As seen in Fig. 8a, the X-axis experiences a tool-to-workpiece displacement of about 160 μm at T1 and T2 and a displacement of about 50 μm at T3 and T4. The warmup causes an X-axis thermal expansion, so the difference in displacements is understandable because T1 and T2 have X-axis values that are about 3.6 times greater than those for T3 and T4. Also, as seen in Fig. 8b, all errors have magnitudes within 10 μm.

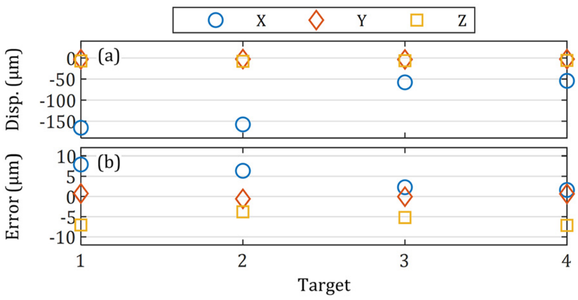

Fig. 8. For an X-axis warmup, (a) displacements measured by the CSs and (b) errors of the new method in all directions for all four targets.

5.3. Thermal drift models

Models were created for one case of simulated drift (Case 3 with 50.8 μm displacements) and for one case of real thermal drift (X-axis warmup), based on the generic model in Sec. 3. Table 1 reveals the dominance of the positional error changes (ΔE_X, ΔE_Y, and ΔE_Z) of about 50 μm among the solution parameters for Model A and the dominance of the change of X-axis thermal expansion ($\Delta\alpha_X$) of about −250 μm/m among the solution parameters for Model B. Those dominant values are shown in bold text in Table 1. Because Model A is for Case 3 with commanded displacements of 50.8 μm, the modeled displacements of about 50 μm are explained. Similarly, because Model B is for the X-axis warmup, the significant change of X-axis thermal expansion is reasonable.

Table 1
Model parameters for simulated thermal drift from commanded three-axis displacements of 50.8 μm and real thermal drift from X-axis warmup.

Model	ΔE_X (μm)	ΔE_Y (μm)	ΔE_Z (μm)	ΔE_A (μrad)	ΔE_B (μrad)	ΔE_C (μrad)	ΔE_{X0Y} (μrad)	$\Delta\alpha_X$ (μm/m)	$\Delta\alpha_Y$ (μm/m)
A†	**50.6**	**50.2**	**46.4**	2.4	−7.0	0.2	−1.4	0.4	4.6
B‡	−14.9	−3.6	−10.8	−5.4	1.2	0.2	4.5	−**247.2**	3.5

† Model A is the model for commanded three-axis displacements of 50.8 μm.
‡ Model B is the model for real thermal drift from X-axis warmup.

6. Conclusions

A new method is proposed to measure thermal drift in near real-time within machine tools. A wireless microscope within a tool holder in the spindle is used to capture videos of high-contrast targets attached to the worktable. For each target, one video is captured during spindle rotation and another video is captured during translation. Image analysis yields the three-dimensional displacements at each target. Experiments with simulated or real thermal drift verify that the method measures micrometer-level tool-to-workpiece thermal drift for compensation purposes.

The proposed method is fast, accurate, inexpensive, non-invasive, and practical for industrial adoption. The microscope can be installed in a tool-holder carousel for automated usage and the targets can be miniaturized, even to be on the worktable sides to not affect machining setups. Future work includes improvement of the microscope assembly for thermal insensitivity, testing with increased targets, use of other high-contrast targets, uncertainty analysis, and integration with machine tool controllers.

Declaration of Competing Interest

The authors declare that they have no known competing financial interests or personal relationships that could have appeared to influence the work reported in this paper.

Acknowledgments

The authors thank the Fabrication Technology Office (NIST), especially Casey Shatzley, for their outstanding contributions with the experimental setup. R.L., E.K., and Z.L. appreciate the support from the U.S. Dept. of Commerce (Award 70NANB22H180).

References

[1] Mayr J, et al. (2012) Thermal Issues in Machine Tools. *CIRP Annals - Manufacturing Technology* 61(2):771–791.
[2] Bryan J (1990) International Status of Thermal Error Research (1990). *CIRP Annals - Manufacturing Technology* 39(2):645–656.
[3] Neugebauer R, Drossel W-G, Ihlenfeldt S, Richter C (2012) Thermal Interactions Between the Process and Workpiece. *Procedia CIRP* 4:63–66.
[4] Donmez MA, Hahn MH, Soons JA (2007) A Novel Cooling System to Reduce Thermally-Induced Errors of Machine Tools. *CIRP Annals - Manufacturing Technology* 56(1):521–524.
[5] Spur G, Hoffmann E, Paluncic Z, Benzinger K, Nymoen H (1988) Thermal Behaviour Optimization of Machine Tools. *CIRP Annals - Manufacturing Technology* 37 (1):401–405.
[6] Jedrzejewski J, Kwasny W, Kowal Z, Modrzycki W (2008) Precise Model of HSC Machining Centre for Aerospace Parts Machining. *Journal of Machine Engineering* 8(3):29–41.
[7] Weck M, McKeown P, Bonse R, Herbst U (1995) Reduction and Compensation of Thermal Errors in Machine Tools. *CIRP Annals - Manufacturing Technology* 44 (2):589–598.
[8] Brecher C, Esser M, Witt S (2009) Interaction of Manufacturing Process and Machine Tool. *CIRP Annals - Manufacturing Technology* 58(2):588–607.
[9] Mayr J, Blaser P, Ryser A, Hernandez-Becerro P (2018) An Adaptive Self-Learning Compensation Approach for Thermal Errors on 5-Axis Machine Tools Handling an Arbitrary Set of Sample Rates. *CIRP Annals - Manufacturing Technology* 67(1):551–554.
[10] Zimmermann N, Lang S, Blaser P, Mayr J (2020) Adaptive Input Selection for Thermal Error Compensation Models. *CIRP Annals - Manufacturing Technology* 69 (1):485–488.
[11] Irino N, Shimoike M, Mori K, Yamaji I, Mori M (2020) A Vision-Based Machine Accuracy Measurement Method. *CIRP Annals - Manufacturing Technology* 69 (1):445–448.
[12] Fujishima M, Narimatsu K, Irino N, Mori M, Ibaraki S (2019) Adaptive Thermal Displacement Compensation Method Based on Deep Learning. *Cirp Journal of Manufacturing Science and Technology* 25:22–25.
[13] Chalfoun J, Majurski M, Dima A, Halter M, Bhadriraju K, Brady M (2016) Lineage Mapper: A Versatile Cell and Particle Tracker. *Scientific Reports* 6(1):36984.
[14] Pertuz S, Puig D, Garcia MA (2013) Analysis of Focus Measure Operators for Shape-From-Focus. *Pattern Recognition* 46(5):1415–1432.